PCCP

Accepted Manuscript

This is an *Accepted Manuscript*, which has been through the Royal Society of Chemistry peer review process and has been accepted for publication.

Accepted Manuscripts are published online shortly after acceptance, before technical editing, formatting and proof reading. Using this free service, authors can make their results available to the community, in citable form, before we publish the edited article. We will replace this *Accepted Manuscript* with the edited and formatted *Advance Article* as soon as it is available.

You can find more information about *Accepted Manuscripts* in the Information for Authors.

Please note that technical editing may introduce minor changes to the text and/or graphics, which may alter content. The journal's standard Terms & Conditions and the Ethical guidelines still apply. In no event shall the Royal Society of Chemistry be held responsible for any errors or omissions in this *Accepted Manuscript* or any consequences arising from the use of any information it contains.

ROYAL SOCIETY OF CHEMISTRY

www.rsc.org/pccp

Journal Name

ARTICLE TYPE

Cite this: DOI: 10.1039/xxxxxxxxxx

Solid-liquid critical behavior of a cylindrically confined Lennard-Jones fluid

Kenji Mochizuki,† and Kenichiro Koga,‡

Received Date
Accepted Date

DOI: 10.1039/xxxxxxxxxx

www.rsc.org/journalname

Extensive molecular dynamics simulations have been performed to study the phase behavior of Lennard-Jones particles confined in a quasi-one-dimensional hydrophobic nanopore. We provide unambiguous evidences for a solid-liquid critical point by investigating (i) isotherms in the pressure-volume plane, (ii) the spontaneous solid-liquid phase separation below a certain temperature, (iii) diverging heat capacity and isothermal compressibility as a certain point is approached, (iv) continuous change of dynamical and structural properties above the point, (v) the finite-size scaling analysis of the density distribution below and above the point. The result combined with earlier studies of confined water suggests that the solid-liquid critical point is not uncommon in quasi-one- and quasi-two-dimensional fluids.

1 Introduction

Since the introduction of the term 'critical point' by Andrews to describe the state where the liquid and gaseous phases lose their separate identities,[1,2] many different kinds of the critical points have been identified or reported, including the liquid-liquid critical point in one-component fluids.[3–8] However, there is a class of the critical points that have not been found so far in experiment. That is, the critical point at which a solid-liquid phase boundary terminates. The non-existence of solid-liquid critical points is commonly explained by the famous symmetry argument: the symmetry cannot change continuously between a crystalline solid and a fluid[1,9]. The argument excludes a thermodynamic path from the liquid to the solid phase without any discontinuity. Nevertheless, there are a number of computer-simulation studies demonstrating that freezing/melting may occur continuously as well as discontinuously in quasi-one- and quasi-two-dimensional systems.[10–14] Very recently, we have provided compelling evidences of the solid-liquid critical phenomena, and a molecular-level mechanism of the continuous melting, for a model of water confined in quasi-one-dimensional hydrophobic nanopores.[15]

There remain unresolved questions as regards the solid-liquid critical phenomena found in molecular simulations, and one of the important issues is what makes the intriguing phenomena possible: whether or not the orientation-dependent intermolecular interaction such as hydrogen bonding is necessary, or the external field that confines molecules in a narrow cylinder or slit is sufficient. It is known that a simple fluid, consisting of Lennard-Jones particles, confined in a smooth cylindrical pore exhibits both continuous and discontinuous freezing,[11] but whether or not the system exhibits the properties characteristic of critical phenomena has been little studied. Here we investigate the confined simple fluid focusing on changes in the structural, dynamic, and thermodynamic properties along isobaric and isothermal paths in between those along which discontinuous and continuous freezing are observed. We then propose a phase diagram which contains solid-liquid phase boundaries terminating at what seems to be the solid-liquid critical point, and discuss the possibility of the solid-liquid critical point.

2 Methods

We performed molecular dynamics simulations of a canonical ensemble (NVT-MD) and an isothermal-isobaric ensemble (NPT-MD) of a model of argon in a carbon nanotube. The LJ size and energy parameters of argon are $\sigma = 3.4$ Å and $\varepsilon/k_B = 120$ K with k_B Boltzmann's constant. The argon-argon interaction is smoothly truncated by applying a switching function[16] from 6.75 Å to 8.75 Å. The interaction between an argon particle and the inner surface of the tube is modeled by a potential function of the distance of the particle from the tube axis alone: the function is obtained by integrating the LJ 12-6 potential over the cylindrical surface, assuming a uniform distribution of carbon atoms of a nanotube on its cylindrical surface.[15,17] The LJ parameters of the argon-carbon interaction is taken to be $(\sigma+\sigma_c)/2$ and $\sqrt{\varepsilon\varepsilon_c}$ with σ_c=3.4 Å and ε_c/k_B=28.0 K. The surface area density is that of carbon atoms in a single-walled carbon nanotube. The tube diameter D is 12.0 Å, a value close to that of the armchair (9, 9)

Department of Chemistry, Faculty of Science, Okayama University, Okayama 700-8530, Japan
† mochizuki@okayama-u.ac.jp
‡ koga@okayama-u.ac.jp

Physical Chemistry Chemical Physics Accepted Manuscript

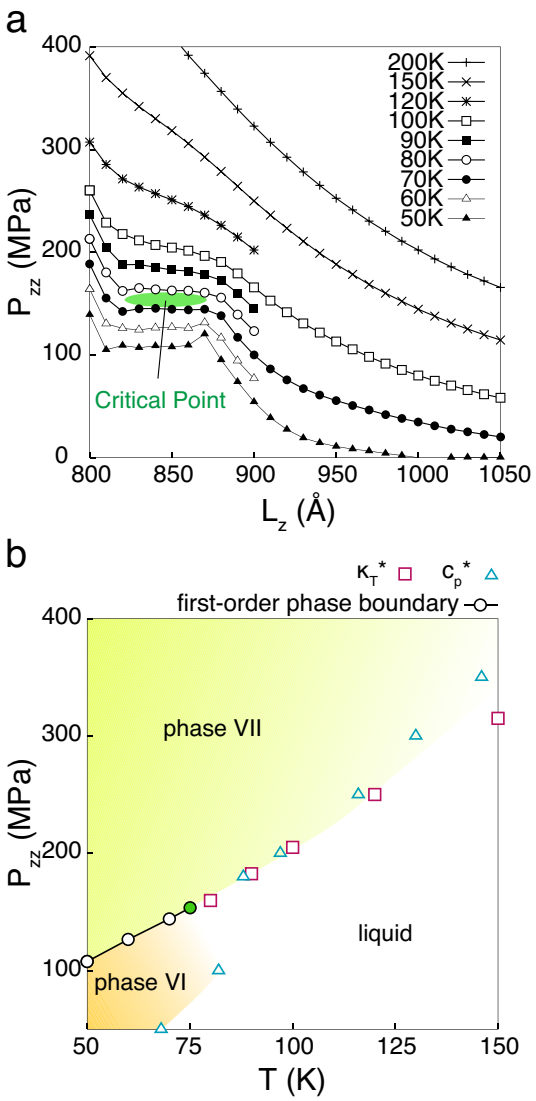

Fig. 1 (a) Isotherms in the "pressure-volume" plane. The green oval indicates the region where the critical point is presumed present. (b) T-P_{zz} phase diagram. The first-order phase boundary, loci of maximum heat capacity c_p^*, and those of isothermal compressibility κ_T^* are shown. The green circle marks the location of the solid-liquid critical point.

single-walled carbon nanotube. A periodic boundary condition is imposed in the axial direction (z-axis) of the nanotube.

In the NVT-MD simulations, the tube length L_z is fixed to a value ranging from 800 to 1050 Å and the number N of the LJ particles is 1000. In the NPT-MD simulations, L_z fluctuates around the mean value determined by N, D, P_{zz}, and T, where P_{zz} is the pressure tensor parallel to the z-axis, and the finite-size scaling analysis is performed with N=200, 400 and 600 and other analyses with N=400. The temperature T and the internal axial pressure P_{zz} are controlled using the modified Nośe-Andersen's method.[18] Trajectories of the confined LJ fluid are generated by the Gear predictor-corrector method with a time step of 0.5 fs. For each state point, the equilibration run of 20 ns is followed by the production run for analyses: the length is 30-80 ns for the NVT-MD simulations, 100 ns for most cases of

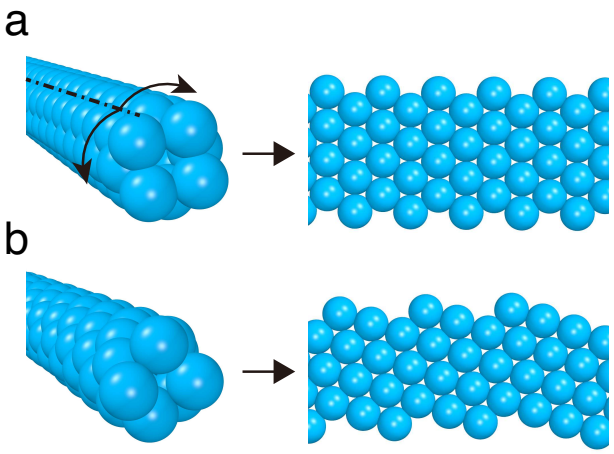

Fig. 2 Inherent structures of (a) solid phase VII obtained from the NVT-MD trajectory at T = 50 K and L_z = 800 Å and (b) solid phase VI at 50 K and 900 Å. The side views and unrolled structures are shown.

the NPT-MD simulations, and extended to 1 μs for the finite-size scaling analysis. The instantaneous configurations are used for the analyses except for the snapshots in Fig. 2. For the latter, we use the inherent structures, i.e., the structures obtained by applying the constant-volume steepest descent method to the instantaneous structures visited by the trajectories.

3 Results and Discussion

In Fig. 1(a) we show isotherms in the "pressure-volume" plane. At low temperatures, the isotherms have a horizontal segment where P_{zz} is independent of L_z, i.e., $dP_{zz}/dL_z = 0$. This indicates that a phase separation takes place under these conditions (in small systems, a van der Waals loop will appear[19,20]). At high temperatures, the slope of the isotherms is always negative, $dP_{zz}/dL_z < 0$. A critical point can be located between the highest-temperature isotherm with $dP_{zz}/dL_z = 0$ and the lowest-temperature isotherm without the horizontal portion. Additionally, the existence of two phases can be judged from the local density profile (see below). With this approach a critical point is located at (T_c/K, P_c/MPa) = (75 $\pm$ 5, 153.5 $\pm$ 9.3) in a region indicated by the green mark in Fig. 1(a).

In Fig. 1(b) we plot the T-P_{zz} phase diagram. The first-order phase boundary (coexistence line) is determined from the average P_{zz} of the horizontal portion of each isotherm at a given temperature. The first-order phase boundary at sufficiently low temperatures is that of two distinct solid phases, the so-called *phase VI* and *phase VII* [11]. Their structures are those of close-packed balls in a cylinder and are specified by the roll-up vector of the two-dimensional triangular lattice.[11] Panels (a) and (b) of Fig. 2 illustrate the inherent structures of both phases obtained from NVT-MD runs at L_z = 800 Å and 900 Å respectively, and T=50 K. From these views, we can easily see the regular arrangement of the argon particles and their long-range ordered structures in the axial direction. At higher temperatures up to 75 K the first-order

Physical Chemistry Chemical Physics Accepted Manuscript

This journal is © The Royal Society of Chemistry [year]

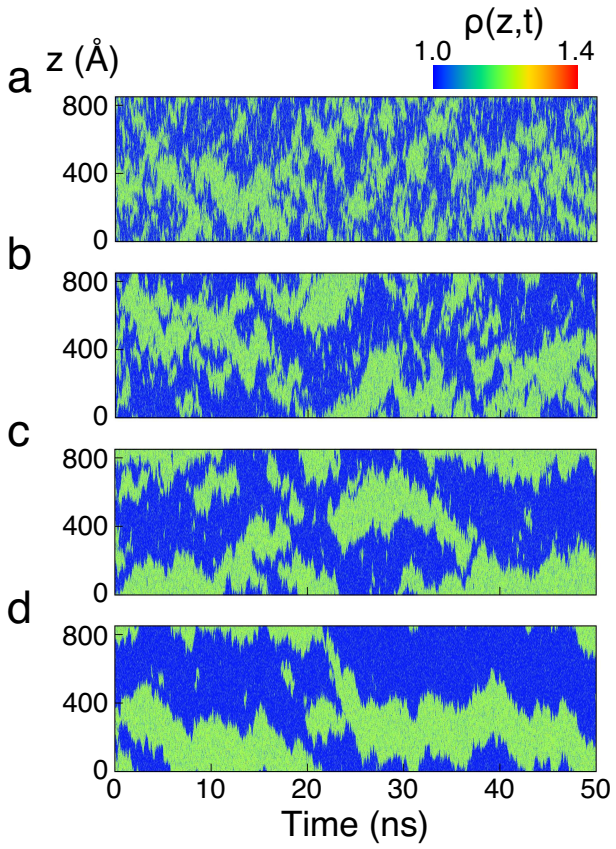

Fig. 3 Time evolution of the scaled local density $\rho(z,t)$ for trajectories at (a) 90 K, (b) 80 K, (c) 70 K and (d) 60 K obtained from the NVT-MD simulations with L_z = 850 Å. The color for $\rho(z,t) < 1.0$ is the same as that for $\rho(z,t) = 1.0$.

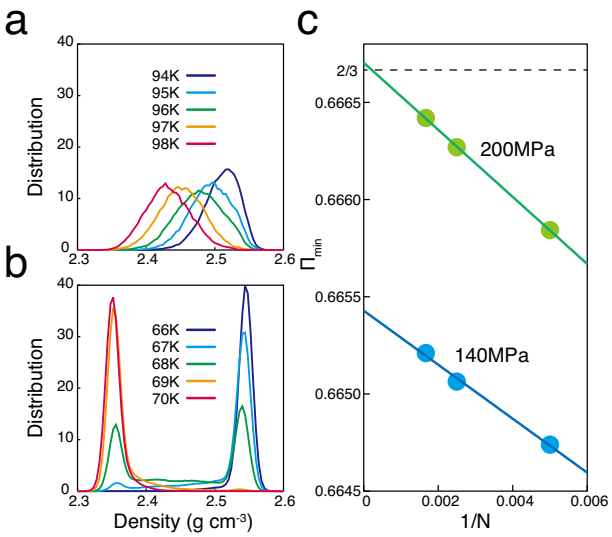

Fig. 4 Finite-size scaling analysis of the Challa-Landau-Binder parameter of the density distribution function $Q(\alpha)$. (a)(b) $Q(\alpha)$ for the system with $N = 600$ at selected temperatures for 200 MPa and 140 MPa, respectively. The temperature at which the $Q(\alpha)$ gives a minimum Π ($\Pi_{\min}$) is 96 K at 200 MPa and 68 K at 140 MPa. (c) Finite-size scaling of $\Pi_{\min}$ along isobars of 140 MPa and 200 MPa: $\Pi_{\min}$ vs. $1/N$. According to a linear fit to the data, $\Pi_{\min}$ approaches 0.6667 (2/3+0.0001) at 200 MPa and 0.6654 at 140 MPa.

boundary is that of solid and liquid phases (as phase VI continuously transforms to a liquid phase with increasing T along the phase boundary) and it ultimately terminates at the solid-liquid critical point. Below the critical point the solid phase VII melts discontinuously whereas at and above the critical point it melts continuously as T increases at a fixed pressure or as P_{zz} decreases at fixed T.

To confirm spontaneous phase separations below the critical temperature and to observe density fluctuations near the critical point, we calculated the scaled local density $\rho(z,t) = (\Delta N(z,t)/\Delta z)/(N/L_z)$,[21] where ΔN is the number of molecules in a cylindrical slab of width Δz (= 5 Å) centered at z and N/L_z is the average number of molecules per unit length. Figures 3(a)–(d) show the time evolution of $\rho(z,t)$ in the NVT-MD simulations at different temperatures (T = 90, 80, 70 and 60 K) and fixed volume (L_z = 850 Å). The initial configuration at $t = 0$ is a randomly generated structure, common to the four NVT-MD runs. Higher and lower values of $\rho(z,t)$ represent phase VII and the disordered phase VI (or liquid phase), respectively. At temperatures above the critical point (80 and 90 K), the system is microscopically inhomogeneous, i.e., there are numerous domains with higher or lower local densities. They are variable in size and tend to form and disappear spontaneously; but they do not grow beyond microscopic sizes. (Such microscopic phase separation above the critical point is also observed in cylindrically confined water.[15]) As T is lowered to T_c the average size of domains becomes larger. When T is close to but below T_c (i.e. at 70 K) there appear most of the time only two domains in the nanotube of length 850 Å although fluctuations are large and more than two appear intermittently. At the lowest investigated temperature (60 K), the two phases are clearly separated with their sizes nearly constant. The spontaneous phase separation observed in the NVT-MD simulation is direct evidence of a first-order phase transition, as it has been for the liquid-liquid phase transition in model water.[19–21]

To ensure the presence of the solid-liquid critical point in the thermodynamics limit, we implement the finite-size analysis of the Challa-Landau-Binder parameter[22–24] $\Pi \equiv 1 - \langle\alpha^4\rangle/3\langle\alpha^2\rangle^2$ of the density $\alpha = N/\pi\sigma_w^2 L_z$, where σ_w (=3.189Å) is the radius at which the potential energy from the wall is zero. Π quantifies the bimodality in the density distribution function $Q(\alpha)$. The minimum of Π (Π_{min}) along an isobar approaches $2/3$ as $N \to \infty$ if $Q(\alpha)$ is unimodal whereas it approaches a value $< 2/3$ if $Q(\alpha)$ is bimodal. We investigate Π for two isobars: P_{zz}=140 MPa which passes slightly below what is conjectured to be the critical point (the green mark in Fig. 1b) and 200 MPa which passes above that point. At 140 MPa, NPT-MD runs are performed for systems of N=200, 400 and 600 at temperatures between 65 and 72 K, each with 1μs production run. Very long MD runs are required to observe phase flipping between the solid and liquid. At 140 MPa and 68 K, for example, fifteen independent freezing events (and the corresponding melting events) are observed in 1 μs of the MD run with $N = 400$. At 200 MPa, NPT-MD runs are performed

Physical Chemistry Chemical Physics Accepted Manuscript

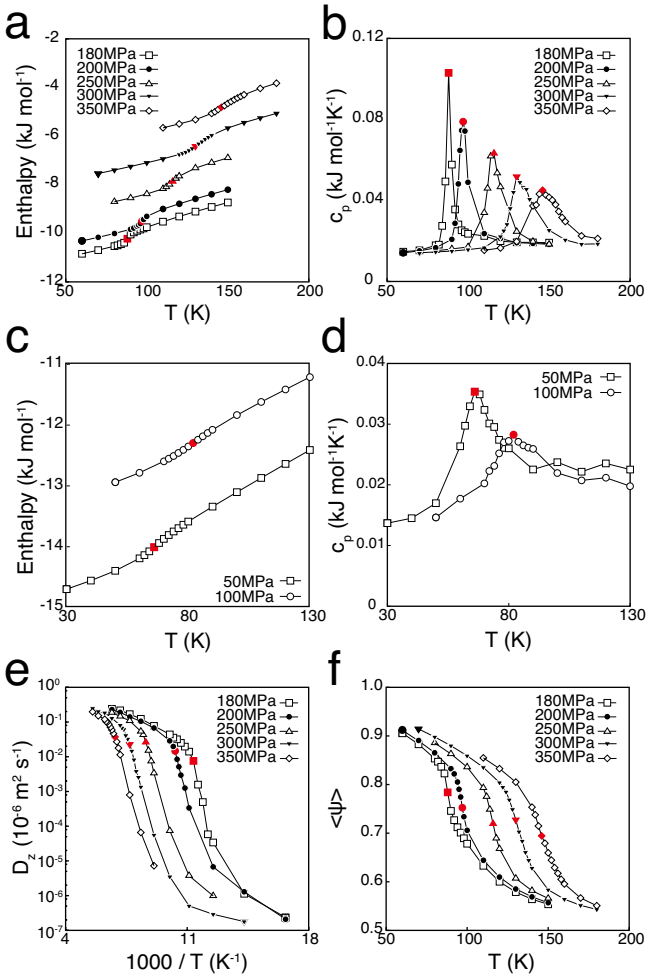

Fig. 5 Temperature (T) dependence of (a)(c) the configurational part of the enthalpy $H = U + P_{zz}V$, (b) (d) the isobaric specific heat capacity c_p, (e) the diffusion coefficient along the tube axis and (f) the average bond order parameter. The isobars in (a)(b)(e) and (f) are the paths of continuous freezing into phase VII, whereas those in (c) and (d) are the paths of continuous freezing into phase VI. Red circles indicate the temperature of maximum heat capacity T^* along each isobar.

for the systems at T between 90 and 100 K, now 100 ns each. As shown in Fig. 4(a)(b), at 200 MPa $Q(\alpha)$ is unimodal at any temperatures while $Q(\alpha)$ becomes bimodal at some temperatures at 140 MPa. The parameter $\Pi(T)$ at fixed pressure takes a minimum value Π_{min} at the temperature where the deviation of $Q(\alpha)$ from a Gaussian is largest. Evaluation of Π_{min} is done by choosing the interval of T to be 0.5 K for 140 MPa and 1 K for 200 MPa near the temperature of Π_{min}. Fig. 4(c) shows the finite-size behavior of Π_{min}. The Π_{min} at 200 MPa approaches $2/3+0.0001$ linearly with $1/N$, indicating the absence of a first-order phase transition in the thermodynamic limit. On the other hand, at 140 MPa Π_{min} approaches a value significantly smaller than 2/3, proving the presence of a first-order phase transition.

To investigate the nature of the continuous solid-liquid phase transformations, we perform long-time NPT-MD simulations of the $N = 400$ system at states along the isobaric paths. First, we evaluate the configurational part of the isobaric heat capacity c_p from $(\overline{H^2} - \overline{H}^2)/k_B T^2$, which describes the fluctuations in the configurational part H of the enthalpy:$U + P_{zz}V$ with U the potential energy of the entire system and $V \equiv \pi\sigma_w^2 L_z$ the inner volume of the tube. Plotted in panels (a) and (b) of Fig. 5 are $H(T)$ and $c_p(T)$ at P_{zz}= 180, 200, 250, 300 and 350 MPa, where the system undergoes continuous freezing to phase VII. There is a maximum $c_p{}^*$ of the heat capacity for each isobaric path. The lower the pressure P_{zz}, the larger c_p^* and the lower the temperature T^* of the maximum heat capacity. This result is consistent with the fact that the maximum slope of $H(T)$ at T^* becomes steeper as P_{zz} is reduced. The loci $T^*(P_{zz})$ are smoothly connected with the first-order phase boundary (see the T-P_{zz} phase diagram in Fig. 1(b)). At P_{zz}= 50 and 100 MPa, too, continuous enthalpy change and maximum heat capacities $c_p{}^*$ are detected during continuous freezing to phase VI (Fig. 5(c) and (d)): The loci $T^*(P_{zz})$ are shown in Fig. 1(b). Along the loci the $c_p{}^*$ increases with decreasing P_{zz}. We have also performed a series of NPT-MD simulations at a pressure below 50 MPa. Upon heating at 0.1 MPa, solid phase VI becomes unstable and separates into clusters at 50 K, suggesting that a vapor phase is stable at that condition. Accordingly, at the diameter D chosen here a liquid-solid (phase VI) discontinuous change is not observed at any pressures. The locus of the continuous changes terminates at a low pressure where the solid or the liquid phase becomes unstable. But at smaller D there would appear the first-order phase boundary which is smoothly connected with the locus of $T^*(P_{zz})$.

Next, the isothermal compressibility $\kappa_T \equiv -(\partial L_z/\partial P_{zz})_T/L_z$ in the axial direction is evaluated along the isotherms in Fig. 1(a). The κ_T is obtained by fitting a third-order polynomial function to each P_{zz}-L_z curve, and determining the locus $P_{zz}^*(T)$ of the maximum isothermal compressibility κ_T^*. The result is shown in the T-P_{zz} phase diagram (Fig. 1(b)). As found for c_p^*, the locus of the maximum compressibility is smoothly connected with the first-order phase boundary. Near the critical point, the loci of c_p^* and κ_T^* converge into a single line, the so-called Widom line[25]. The loci bifurcate as they recede from the critical point, as recently reported in the liquid-liquid critical behavior of supercooled water.[26] Thus, the behaviors of the response function maxima, too, suggest the existence of a solid-liquid critical point in the confined LJ fluid.

We now look at, in the course of continuous freezing to, or melting of, phase VII, how dynamic and structural properties of the LJ particles change. Figure 5(e) shows the temperature dependence of the diffusion coefficient of the LJ particles along the tube axis: $D_z = \lim_{t\to\infty} \overline{|z(t) - z(0)|^2}/2t$. It is the plot of $\log D_z$ vs. $1/T$ for various isobars. There are broadly three stages with different slopes and the slope $d\log D_z/d(1/T)$ is steepest in the second stage, i.e., in the intermediate temperature range, which includes the temperature of c_p^* and κ_T^*. The temperature dependence of D_z may be regarded as the Arrhenius behavior

Physical Chemistry Chemical Physics Accepted Manuscript

This journal is © The Royal Society of Chemistry [year]

over limited high and low temperature ranges, but overall it is non-Arrhenius.

To measure an order parameter of the local structure, we first unroll the instantaneous structure by projecting the positions of particles on the two-dimensional surface of the cylinder of radius r' as shown in Fig. 2. Then we find a two-dimensional structure on the x'-z plane with x' the coordinate along the circumference of the cylinder. We choose $r' = 2\sigma/\pi$ to ensure that four LJ particles at the same z in the solid phase VII are aligned at intervals of σ in the x'-direction. Periodic boundary conditions are assumed in the x' and z directions. We then calculate the local bond order parameter of particle j on the x'-z plane defined as

$$\psi_j = \frac{1}{N_j} \left| \sum_{k=1}^{N_j} \exp(6i\theta_{jk}) \right|,$$

where the sum is over N_j neighbours of particle j, and θ_{jk} is the angle between the vector $\vec{r}_{jk}$ from j to its k-th neighbor and a reference axis (e.g., the x' axis). Two particles are considered neighbours if their separation is less than 5 Å, the location of the first minimum of the two-dimensional radial distribution function. Note that ψ_j becomes 1 when N_j=6 and the six neighbours form a regular hexagon with j at the center. In the close-packed structure of spheres on a plane, $\psi_j = 1$ for any j. The ensemble and time average $\langle\psi\rangle$ is plotted as a function of T for various isobars in Fig. 5(f). As T increases $\langle\psi\rangle$ gradually decreases, an indication of gradual transformation of the ordered structure to disordered one. The change in $\langle\psi\rangle$ is rapid at an intermediate range of temperatures, which coincides with the range over which $\ln D_z$ varies most rapidly, and also with the ranges of maximum heat capacity and compressibility. The temperature range of the intermediate stage shrinks as the critical point is approached. The marked changes in the dynamic and structural properties around the temperature of maximum heat capacity and compressibility are also observed for a model system of cylindrically confined water.[15]

The convergence of the simulation data reported here was confirmed as follows. The production run of MD simulation at each thermodynamic state is divided into blocks of equal length, the block averages of a quantity of interest are obtained, and the standard deviation of the averages is examined. First, we focus on the average pressure at L_z=850 Å and T=80 K in Fig. 1, where the dispersion is expected to be large owing to the critical point. The production run of 30 ns is divided into three blocks of 10 ns each and the standard deviation of the block averages is found to be 0.24 MPa. Second, the accuracy of the minimum of the Challa-Landau-Binder parameter (Π_{min}) for a system of N=600 is evaluated. The temperature at which the density distribution function gives Π_{min} is 96 K at 200 MPa and 68 K at 140 MPa (see Fig. 4). The production runs are divided into four blocks and the estimated standard division of Π is 0.00001 and 0.0001, respectively. Third, we take the simulation data at 180 MPa and 88 K in Fig. 5, where the maximum heat capacity is exhibited. The production run of 80 ns is divided into four blocks of 20 ns each. The estimated standard deviation is 0.02 $\mathrm{kJ\,mol^{-1}}$ for the enthalpy, 0.004 $\mathrm{kJ\,mol^{-1}K^{-1}}$ for the heat capacity, 0.002 $\mathrm{m^2\,s^{-1}}$ for the diffusion coefficient, and 0.007 for the average bond order parameter. Thus, these small standard deviations ensure that the MD simulation runs are sufficiently long for the convergence of quantities reported in this study.

4 Summary

The existence of the solid-liquid critical point in cylindrically confined LJ particles was revealed by investigating the isotherms of pressure, the spontaneous phase separation, and the diverging behaviors of the response functions. Furthermore, the finite-size scaling analysis supports the presence of both first-order and continuous freezing in the thermodynamic limit. With our previous study of cylindrically confined water,[15] we now have two examples of realistic models of fluids in nanopores that exhibit the solid-liquid critical point. The present result indicates that a highly directional intermolecular interaction such as hydrogen bonding is not a necessary condition for the presence of the critical point, although it often plays a crucial role in phase transitions of bulk water.[27–29] Rather, the solid-liquid critical point presumably exists in a variety of quasi-one-dimensional systems (e.g., colloids in microchannels[30–32], fullerenes in nanotubes[33] and biological microstructures[34]) and of quasi-two-dimensional systems (e.g., molecules or colloids confined in a slit pore and those adsorbed on solid surfaces and fluid interfaces).[35–37] It is of great significance to explore solid-liquid critical phenomena in a wider class of realistic systems by numerical simulation. And equally important and extremely valuable are rigorous studies on the necessary condition for the solid-liquid critical point using simple models in various dimensions which may be exactly solvable.[9,38–40]

5 Acknowledgement

This work was supported by a Grant-in-Aid for Scientific Research (KAKENHI) (No. 26888011, 15H05474 and 26287099) and the program for promoting the enhancement of research universities, MEXT. Most of the calculations were performed at the Research Center for Computational Science in Okazaki, Japan.

References

1 H. Stanley, *Introduction to Phase Transitions and Critical Phenomena*, Oxford University Press, 1971.
2 C. Domb, *The critical point: A historical introduction to the modern theory of critical phenomena*, Taylor & Francis, 1996.
3 S. Sastry and C. A. Angell, *Nat. Mater.*, 2003, **2**, 739–743.
4 J. Palmer, F. Martelli, Y. Liu, R. Car, A. Panagiotopoulos and P. Debenedetti, *Nature*, 2014, **510**, 385–388.
5 P. Gallo and F. Sciortino, *Phys. Rev. Lett.*, 2012, **109**, 177801.
6 O. Mishima and H. E. Stanley, *Nature*, 1998, **396**, 329–335.
7 K. Murata and H. Tanaka, *Nat. Commun.*, 2013, **4**, 2844.
8 R. Kurita and H. Tanaka, *Science*, 2004, **306**, 845–848.

Physical Chemistry Chemical Physics Accepted Manuscript

9 L. D. Landau and E. M. Lifshits, *Statistical Physics*, Betterworth-Heinemann, 1980.

10 K. Koga, G. Gao, H. Tanaka and X. Zeng, *Nature*, 2001, **412**, 802–805.

11 K. Koga and H. Tanaka, *J. Chem. Phys.*, 2006, **124**, 131103.

12 H. Huang, S. Kwak and J. Singh, *J. Chem. Phys.*, 2009, **130**, 164511.

13 M. C. Gordillo, B. Martinez-Haya and J. M. Romero-Enrique, *J. Chem. Phys.*, 2006, **125**, 144702.

14 F. J. Duran-Olivencia and M. C. Gordillo, *Phys. Rev. E*, 2009, **79**, 061111.

15 K. Mochizuki and K. Koga, *Proc. Natl. Acad. Sci. U. S. A*, 2015, in press.

16 I. Ohmine, H. Tanaka and P. Wolynes, *J. Chem. Phys.*, 1988, **89**, 5852–5860.

17 D. Takaiwa, I. Hatano, K. Koga and H. Tanaka, *Proc. Natl. Acad. Sci. U. S. A*, 2008, **105**, 39–43.

18 D. C. Rapaport, *The Art of Molecular Dynamics Simulations*, Cambridge Univ. Press, Cambridge, 1997.

19 P. Poole, F. Sciortino, U. Essmann and H. Stanley, *Nature*, 1992, **360**, 324–328.

20 M. Yamada, S. Mossa, H. Stanley and F. Sciortino, *Phys. Rev. Lett.*, 2002, **88**, 195701.

21 T. Yagasaki, M. Matsumoto and H. Tanaka, *Phys. Rev. E*, 2014, **89**, 020301.

22 M. S. Chella, D. P. Landau and K. Binder, *Phys. Rev. B*, 1986, **34**, 1841–1852.

23 T. Kesselring, G. Franzese, S. Buldyrev, H. Hermann and H. Stanley, *Sci. Rep.*, 2012, **2**, 474.

24 V. Bianco and G. Franzese, *Sci. Rep.*, 2014, **4**, 4440.

25 L. Xu, P. Kumar, S. Buldyrev, S.-H. Chen, P. Poole, F. Sciortino and H. Stanley, *Proc. Natl. Acad. Sci. U. S. A*, 2005, **102**, 16558–16562.

26 J. Luo, L. Xu, E. Lascaris, H. E. Stanley and S. V. Buldyrev, *Phys. Rev. Lett.*, 2014, **112**, 135701.

27 M. Matsumoto, S. Saito and I. Ohmine, *Nature*, 2002, **416**, 409–413.

28 K. Mochizuki, M. Matsumoto and I. Ohmine, *Nature*, 2013, **498**, 350–354.

29 K. Mochizuki, K. Himoto and M. Matsumoto, *Phys. Chem. Chem. Phys.*, 2014, **16**, 16419–16425.

30 J. H. Moon, S. Kim, G. R. Yi, Y. H. Lee and S. M. Yang, *Langmuir*, 2004, **20**, 2033–2035.

31 F. Li, X. Badel, J. Linnros and J. B. Wiley, *J. Am. Chem. Soc.*, 2005, **127**, 3268–3269.

32 M. Tymczenko, L. F. Marsal, T. Trifonov, I. Rodriguez, F. Ramiro-Manzano, J. Pallares, A. Rodriguez, R. Alcubilla and F. Meseguer, *Adv. Mater.*, 2008, **20**, 2315–2318.

33 A. N. Khlobystov, D. A. Britz, A. Ardavan and G. A. D. Briggs, *Phys. Rev. Lett.*, 2004, **92**, 245507.

34 R. O. Erickson, *Science*, 1973, **181**, 705–716.

35 S. Han, M. Choi, P. Kumar and H. Stanley, *Nat. Phys.*, 2010, **6**, 685–689.

36 R. Radhakrishnan, K. Gubbins and M. Sliwinska-Bartkowiak, *Phys. Rev. Lett.*, 2002, **89**, 076101.

37 J. C. Johnston, N. Kastelowitz and V. Molinero, *J. Chem. Phys.*, 2010, **133**, 154516.

38 A. Cuesta J A, Sánchez, *J. Stat. Phys.*, 2004, **115**, 869–893.

39 C. J. Thompson, in *Classical equilibrium statistical mechanics*, Clarendon Press, 1988, p. 50 and 138.

40 F. J. Dyson, *Commun. math. Phys.*, 1969, **12**, 91–107.

Physical Chemistry Chemical Physics Accepted Manuscript

This journal is © The Royal Society of Chemistry [year]